

Melnikov-Based Dynamical Analysis of Microcantilevers in Scanning Probe Microscopy

M. ASHHAB, M. V. SALAPAKA, M. DAHLEH, and I. MEZIĆ

Mechanical and Environmental Engineering Department, University of California at Santa Barbara, Santa Barbara, CA 93106, U.S.A.

(Received: 5 May 1998; accepted: 19 April 1999)

Abstract. We study the dynamical behavior of a microcantilever-sample system that forms the basis for the operation of atomic force microscopes (AFM). We model the microcantilever by a single mode approximation. The interaction between the sample and the cantilever is modeled by a Lennard–Jones potential which consists of a short-range repulsive potential and a long-range van der Waals (vdW) attractive potential. We analyze the dynamics of the cantilever sample system when the cantilever is subjected to a sinusoidal forcing. Using the Melnikov method, the region in the space of physical parameters where chaotic motion is present is determined. In addition, using a proportional and derivative controller, we compute the Melnikov function in terms of the parameters of the controller. Using this relation, controllers can be designed to selectively change the regime of dynamical interaction.

Keywords: Atomic force microscopy, chaotic behavior, Melnikov method, microcantilevers.

1. Introduction

In 1986, Calvin Quate, Christopher Gerber and G. Binnig built the Atomic Force Microscope which revolutionized microscopy [1]. With its advent, images of surfaces of materials, conducting or not, at the atomic scale were obtained with relative ease. Since then, the basic operating principle of the atomic force microscope has been used for measuring various physical properties of materials other than the surface force profile. It has had a significant impact on the semiconductor industry where it is routinely employed to measure the roughness of silicon wafers [2, 3]. It is widely used by biologists to image DNA strands [4] and monitoring RNA activity [5]. Recently, atomic force microscopy principles have been used to obtain thermal profiles of samples with subkelvin resolution [6]. Other applications where similar techniques have yielded considerable dividends, are in measuring magnetic fields [7, 8] and in measuring electrical properties of materials [9, 10]. The operating principles of the various applications mentioned are given in [11]. All of these methods share the basic mechanism of a microcantilever interacting with a sample.

A schematic representation of the atomic force microscope is shown in Figure 1. A typical AFM consists of a microcantilever, a sample positioner, a detection system and a control system. A laser incident on the top surface of the cantilever which is reflected into a photodiode array is used to detect the motion of the cantilever. When the sample is close enough to the cantilever, it exerts a large enough force to deflect the microcantilever and causes a detectable signal to be registered at the photodiode array. The control system decides the position of the sample based on the photodiode output.

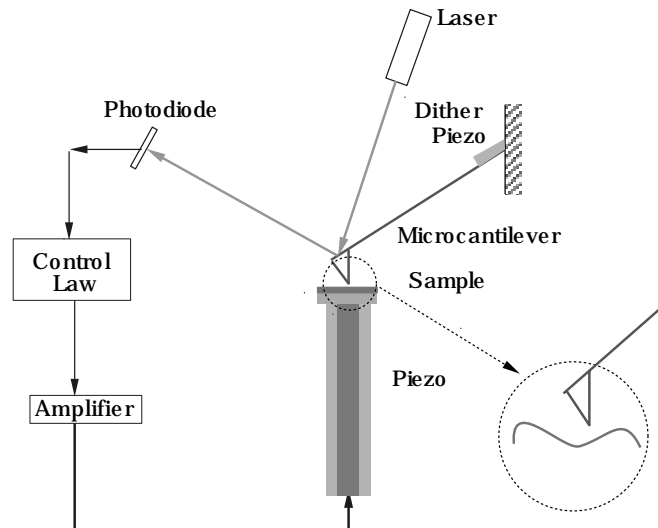


Figure 1. Schematic representation of the atomic force microscope setup.

In one of the most popular modes of imaging, the *tapping mode*, the cantilever is vibrated near its resonant frequency by a dither piezo (see Figure 1). The behavior of the cantilever under such a forcing depends on the sample surface and material characteristics. By monitoring the vibration of the cantilever, information on the sample is obtained.

As is evident, the cantilever is central to the operation of the atomic force microscope. Imperative to the correct interpretation of data and for enhancing the performance of an atomic force microscope is a thorough analysis of the cantilever and its interaction with the sample. The cantilever-sample interaction, as will be demonstrated, is highly nonlinear. Standard techniques of using a linear model fail to describe the behavior of the cantilever in the *tapping mode* operation because, in this mode, the cantilever moves through the whole range of the nonlinear interaction force. In earlier studies [12] it has been demonstrated that even with a simpler interaction force complex behavior of the cantilever is possible. The analytical results are corroborated by experimental evidence (see, for example, [13]).

The impetus in the atomic force imaging technology is towards faster speeds of operation and higher resolution. There is considerable activity in using smaller and stiffer cantilevers to obtain faster imaging using the *tapping mode* [14]. This makes it essential to study the range of parameters of the cantilever under which the cantilever detection system performs predictably. Also, with the introduction of newer cantilevers with properties hitherto not possible, newer modes of imaging can be devised to obtain material characteristics.

In this paper, the cantilever is modeled as a single spring-mass-damper system. A nonlinear dynamic model is developed for the cantilever-sample interaction which has the experimentally observed features of long-range attractive forces and short-range repulsive forces. This model is derived from the Lennard–Jones potential for the interaction between two molecules. Based on this model, the behavior of the cantilever under a sinusoidal forcing is studied. In particular, the phase portrait of the dynamics is obtained for a range of cantilever-sample distances. It is shown that in a relevant range of operation, the phase portrait consists of two homoclinic orbits filled with periodic orbits. The fate of these orbits under a sinusoidal forcing and damping is studied using the Melnikov method. This method is employed to delineate the

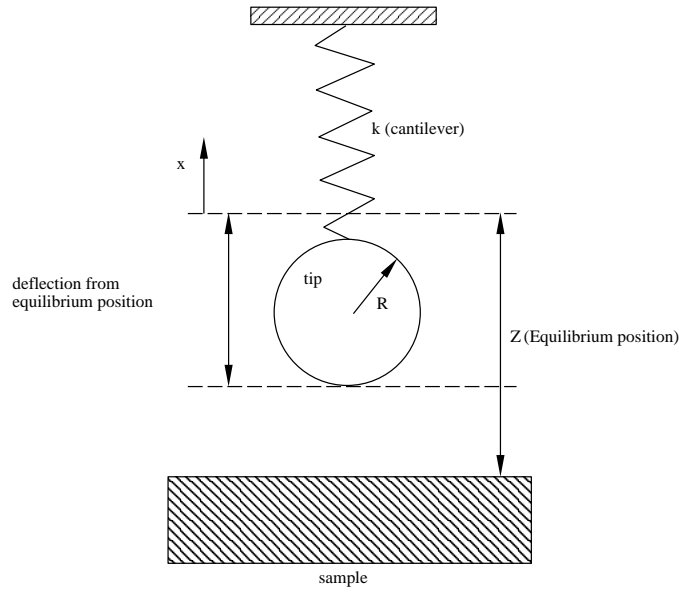


Figure 2. Tip-sample model.

region in the parameter space when chaotic dynamics is present. It is shown that feedback control can be utilized to obtain desirable behavior.

The paper is organized as follows. In Section 2, the model of the cantilever and the cantilever-sample interaction is derived. In Section 3, the dynamics are analyzed under no external forcing. In the next section, the Melnikov function is derived and the dynamics are studied when there is an external sinusoidal forcing with damping present. Finally, in Section 5, we conclude and present directions for future research.

2. Model Description

The achievable sensitivity and resolution of an AFM are largely determined by the cantilever. In most AFM imaging, the cantilever is modeled as a spring-mass-damper system. In this work, the model employed is described by Figure 2, where the tip is modeled as a sphere of radius R and mass m , suspended by a spring of stiffness k . The cantilever-sample distance is characterized by Z which is the distance between the equilibrium position of the cantilever and the sample when only the gravity is acting on it. The cantilever position is given by x measured from the equilibrium position. This model is similar to the one used in [16].

The parameters of the cantilever model (stiffness, mass and damping) can be found in a straightforward manner by the methods indicated in [17]. The cantilever-sample interaction model is based on the Lennard–Jones potential [18] between two molecules, which is given by

$$w(r) = \frac{c_1}{r^{12}} - \frac{c_2}{r^6} = 4\beta \left[\left(\frac{\sigma}{r} \right)^{12} - \left(\frac{\sigma}{r} \right)^6 \right], \quad (1)$$

where r is the distance between the two molecules, σ is the molecular diameter, c_1 and c_2 are interaction constants, and $-\beta$ is the minimum of the potential (see Figure 3). Typical values of σ and β are 0.3 \AA and $20 \times 10^{-21} \text{ J}$, respectively. We now evaluate the interaction potential

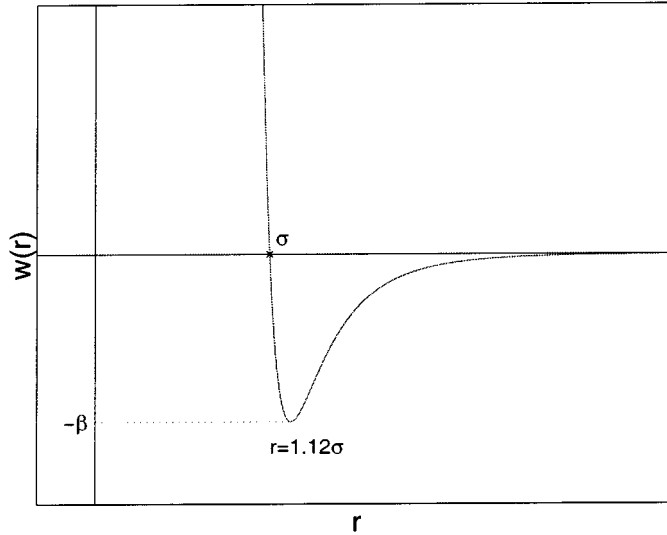


Figure 3. Intermolecular Lennard-Jones potential.

between a single molecule placed at a distance z from the sample (see Figure 4). Suppose the sample has ρ_2 molecules per unit volume and suppose the sphere has ρ_1 molecules per unit volume. The net number of molecules in an annular region in the sample of thickness dy and width dx at a distance y is given by $2\pi\rho_2y dx dy$. Thus, the interaction energy is given by

$$\begin{aligned}
 w(z) &= \int_{x=z}^{\infty} \int_{y=0}^{\infty} 2\pi\rho_2y \left(\frac{c_1}{(x^2+y^2)^6} - \frac{c_2}{(x^2+y^2)^3} \right) dy dx \\
 &= 2\pi\rho_2c_1 \int_{x=z}^{\infty} dx \int_{y=0}^{\infty} \frac{y dy}{(x^2+y^2)^6} - 2\pi\rho_2c_2 \int_{x=z}^{\infty} dx \int_{y=0}^{\infty} \frac{y dy}{(x^2+y^2)^3} \\
 &= \frac{2\pi\rho_2c_1}{90z^9} - \frac{2\pi\rho_2c_2}{12z^3}.
 \end{aligned} \tag{2}$$

We now compute the sphere-surface interaction energy. As shown in Figure 5, all of the molecules that are at a distance $x + D_{ss}$ from the surface lie in a circular section of area πy^2 and thickness dx . The number of molecules in this section is $\rho_1\pi y^2 dx = \rho_1\pi(2R - x)x dx$. Using Equation (2), the interaction energy is given by

$$W(D_{ss}) = \int_{x=0}^{x=2R} \rho_1\pi(2R - x)x \left(\frac{2\pi\rho_2c_1}{90(D_{ss} + x)^9} - \frac{2\pi\rho_2c_2}{12(D_{ss} + x)^3} \right) dx.$$

In the atomic force microscope applications that we are considering, $R \gg D_{ss}$ as explained in [16]. A typical value of R is 1500\AA , while the tip equilibrium position allows values around 120\AA . Under this assumption, $2Rx \gg x^2$ and only small values of x ($x \approx D_{ss}$) contribute to

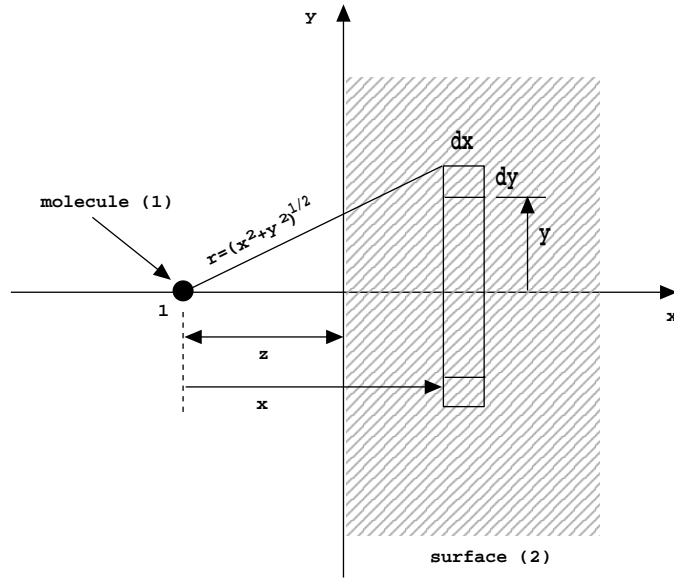


Figure 4. Molecule-flat surface interaction.

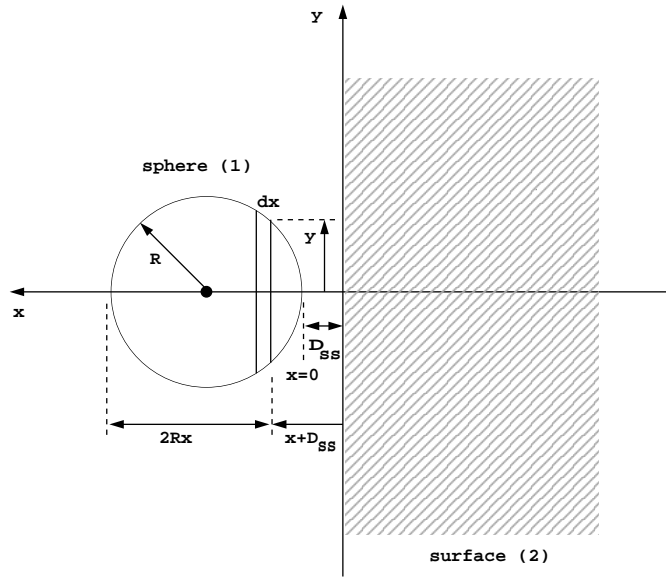


Figure 5. Sphere-flat surface interaction.

the integral. Thus, we can write

$$\begin{aligned}
 W(D_{ss}) &= \frac{2A_1}{90} \int_{x=0}^{x=\infty} \frac{2Rx}{(D_{ss} + x)^9} dx - \frac{2A_2}{12} \int_{x=0}^{x=\infty} \frac{2Rx}{(D_{ss} + x)^3} dx \\
 &= \frac{A_1 R}{1260 D_{ss}^7} - \frac{A_2 R}{6 D_{ss}},
 \end{aligned} \tag{3}$$

where $A_1 = \pi^2 \rho_1 \rho_2 c_1$ and $A_2 = \pi^2 \rho_1 \rho_2 c_2$ are the Hamacker constants for the repulsive and attractive potentials, respectively.

Thus, the tip-sample interaction is modeled by an interaction potential given by

$$V(x, Z) = \frac{A_1 R}{1260(Z+x)^7} - \frac{A_2 R}{6(Z+x)} + \frac{1}{2} k x^2. \quad (4)$$

The net energy of the system scaled by the effective mass m of the cantilever is denoted by $H(x, \dot{x}, Z)$, where

$$H(x, \dot{x}, Z) = \frac{1}{2} \dot{x}^2 + \frac{1}{2} \omega_1^2 x^2 - \frac{D \omega_1^2}{(Z+x)} + \frac{\sigma^6 D \omega_1^2}{210(Z+x)^7}, \quad (5)$$

with $\omega_1 = \sqrt{k/m}$ and $D = A_2 R/6k$. Note that H is the Hamiltonian of the system. Also, H is a constant of the dynamics (invariant of motion) since there is no dissipation. We let $x_1 = x$ and $x_2 = \dot{x}$. The dynamics of the tip-sample system derived from the above Hamiltonian is given below ($\dot{x}_1 = \partial H / \partial x_2$ and $\dot{x}_2 = -(\partial H / \partial x_1)$)

$$\dot{x}_1 = x_2, \quad (6)$$

$$\dot{x}_2 = -\omega_1^2 x_1 - \frac{D \omega_1^2}{(Z+x_1)^2} + \frac{\sigma^6 D \omega_1^2}{30(Z+x)^8}. \quad (7)$$

The actual system is both damped and forced and therefore it is not Hamiltonian. We view the damping and external forcing as perturbations to the Hamiltonian system. The trajectories of the Hamiltonian system will be used to study the behavior of the perturbed system.

We now define variables which facilitate the study of the qualitative behavior of the system. We let $T = \omega_1 t$ (timescale) and divide the left and right-hand sides of Equations (6) and (7) by the distance $Z_s = (3/2)(2D)^{1/3}$ (see [12] for a motivation) to get

$$\xi_1' = \xi_2, \quad (8)$$

$$\xi_2' = -\xi_1 - \frac{d}{(\alpha + \xi_1)^2} + \frac{\Sigma^6 d}{30(\alpha + \xi_1)^8}, \quad (9)$$

where

$$\xi_1 = \frac{x_1}{Z_s}, \quad \xi_2 = \frac{x_2}{\omega_1 Z_s}, \quad d = \frac{4}{27}, \quad \alpha = \frac{Z}{Z_s} \quad \text{and} \quad \Sigma = \frac{\sigma}{Z_s}.$$

Typical values of Z_s are around 100\AA . The prime denotes the derivative with respect to T . The Hamiltonian of the system in the nondimensionalized coordinates is given by

$$H(\xi_1, \xi_2, \alpha) = \frac{1}{2} \xi_2^2 + \frac{1}{2} \xi_1^2 - \frac{d}{(\alpha + \xi_1)} + \frac{\Sigma^6 d}{210(\alpha + \xi_1)^7}. \quad (10)$$

3. The Unforced System

In this section, we study the cantilever sample system when there is no other external forcing on the cantilever. The results of this section will be utilized later to analyze the dynamics when the cantilever is subjected to a sinusoidal forcing in the presence of damping. The

cantilever in the presence of the sample is subjected to three different kinds of forces, namely, the spring force, the vdW attractive force which is proportional to the inverse square power of the distance between the tip and the sample, and the repulsive force which is proportional to the inverse eighth power of the distance between the tip and the sample. We define the Lennard–Jones (LJ) force as the sum of the attractive and repulsive forces. It is given by

$$F_{\text{LJ}}(\xi_1) = -\frac{d}{(\alpha + \xi_1)^2} + \frac{\Sigma^6 d}{30(\alpha + \xi_1)^8}, \quad (11)$$

whereas the spring force is given by $F_s(\xi_1) = -\xi_1$. Equating the right-hand sides of Equations (8) and (9) to zero, we have

$$\eta^8(\eta - \alpha) + d\eta^6 - \frac{\Sigma^6 d}{30} = 0 \quad \text{and} \quad \xi_2 = 0, \quad (12)$$

where $\eta := \alpha + \xi_1$ is a redefined distance. Solutions to these equations give the fixed points of the cantilever sample dynamics.

We now study the LJ force shown in Figure 6. In particular, we will find the points at which $-F_{\text{LJ}}$ is zero, maximum or has a minimum slope. The minimum slope of $-F_{\text{LJ}}$ will give a critical value of Σ which splits the analysis into three different cases as we will see in the sequel. Setting Equation (11) equal to zero and solving for ξ_1 yields

$$\xi_{l_{j0}} = \left(\frac{1}{30}\right)^{1/6} (\Sigma) - \alpha = 0.567\Sigma - \alpha. \quad (13)$$

Note that the zero of the LJ force, $\xi_{l_{j0}}$ is very close to the sample since σ is very small. Typical values of Σ are 0.03–0.1. Setting the derivative of Equation (11) equal to zero and solving for ξ_1 gives the point at which $-F_{\text{LJ}}$ is maximum, namely,

$$\xi_{l_{jp}} = \left(\frac{2}{15}\right)^{1/6} \Sigma - \alpha = 0.715\Sigma - \alpha. \quad (14)$$

The difference between $\xi_{l_{jp}}$ and $\xi_{l_{j0}}$ is 0.148Σ indicating the large increase of the slope of $-F_{\text{LJ}}$ as we move from $\xi_{l_{jp}}$ to $\xi_{l_{j0}}$. The increase is large if Σ is relatively small which is the typical case. Next, we find the point at which the slope of the LJ force is minimum. The zero of the second derivative of Equation (11) is given by

$$\xi_{l_{js}} = (0.4)^{1/6} \Sigma - \alpha = 0.858\Sigma - \alpha. \quad (15)$$

The first derivative of $-F_{\text{LJ}}$ at $\xi_{l_{js}}$ is equal to $-(4d/3\sqrt{0.4}\Sigma^3)$. Therefore, the slope of $-F_{\text{LJ}}$ at $\xi_{l_{js}}$ is equal to -1 if and only if

$$\Sigma = \left(\frac{4d}{3\sqrt{0.4}}\right)^{1/3} = 0.678. \quad (16)$$

We denote by Σ_1 the value $(4d/3\sqrt{0.4})^{1/3} = 0.678$. Since $\Sigma = \sigma/Z_s$ and σ is small, at $\Sigma = \Sigma_1$, Z_s is also small (of the same order as σ). Thus, Σ will be equal to Σ_1 if the cantilever is very stiff since Z_s is proportional to the inverse third power of k . Also note that the minimum slope of the negative of the LJ force is less than -1 if $\Sigma < \Sigma_1$ and vice versa.

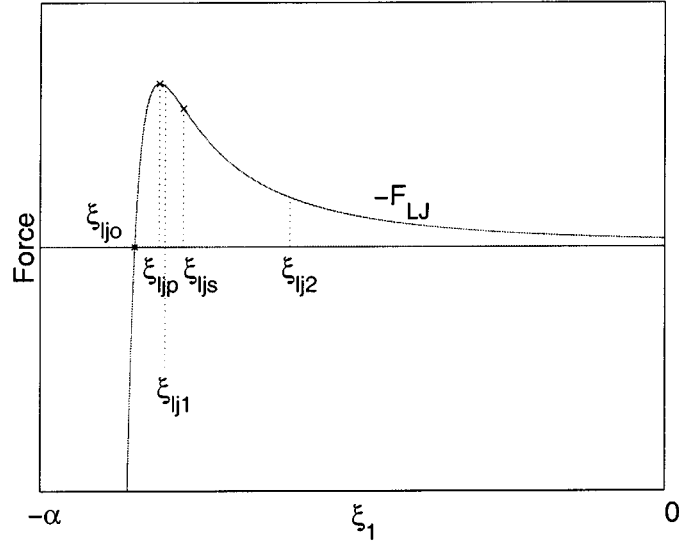


Figure 6. The Lennard–Jones (LJ) force. The positions at which the force is zero and maximum are ξ_{lj0} and ξ_{ljp} , respectively. The force has a minimum slope at the point ξ_{ljs} and slope equal to -1 at the points ξ_{lj1} and ξ_{lj2} when $\Sigma < \Sigma_1$.

At the point $\xi_1 = \xi_{ljs}$, the LJ force is given by

$$F_{LJ}(\xi_{ljs}) = -\frac{d}{(\alpha + \xi_{ljs})^2} + \frac{1}{12} \frac{d}{(\alpha + \xi_{ljs})^2} = -\frac{11}{12} \frac{d}{(\alpha + \xi_{ljs})^2}. \quad (17)$$

At the equilibrium points $F_s = -F_{LJ}$, that is, the following condition must be satisfied

$$-\xi_1 = \frac{d}{(\alpha + \xi_1)^2} - \frac{\Sigma^6 d}{30(\alpha + \xi_1)^8}. \quad (18)$$

3.1. THE CASE $\Sigma < \Sigma_1$

Figure 7 shows the interaction force F_{LJ} for various values of the parameter α assuming that Σ is a given fixed value below Σ_1 . As $\Sigma < \Sigma_1$, the slope of $-F_{LJ}$ at ξ_{ljs} is less than -1 for any α . Thus, the slope is equal to -1 at some point $\xi_1 = \xi_{lj1} \in (\xi_{ljp}, \xi_{ljs})$. Also, there exists $\alpha = \alpha_{sl}$ at which the spring force F_s becomes tangent to $-F_{LJ}$ at the point ξ_{lj1} . In addition, we know that the slope of $-F_{LJ}$ is equal to -1 at some point $\xi_1 = \xi_{lj2} \in (\xi_{ljs}, 0)$. Also, there exists $\alpha = \alpha_{sv} < \alpha_{sl}$ at which the spring force F_s becomes tangent to $-F_{LJ}$ at the point ξ_{lj2} (see Figure 7). The number of intersection points of the curves F_s and $-F_{LJ}$ and therefore the dynamical behavior of the system depend on the value of α . If $\alpha < \alpha_{sv}$ then there is only one intersection point ξ_{cl} as shown in Figure 7. Linearizing the system (8) and (9), we get

$$\begin{pmatrix} \xi_1' \\ \xi_2' \end{pmatrix} = \begin{pmatrix} 0 & 1 \\ -1 + \frac{dF_{LJ}}{d\xi_1}(\xi_1) & 0 \end{pmatrix} \begin{pmatrix} \xi_1 \\ \xi_2 \end{pmatrix}. \quad (19)$$

Since $\xi_{cl} \in (\xi_{lj0}, \xi_{ljs})$, the linearized system has purely imaginary eigenvalues at $\xi_1 = \xi_{cl}$. Therefore, the fixed point $(\xi_{cl}, 0)$ is a center. The corresponding phase portrait of the system is shown in Figure 8. Away from the surface, the net force on the tip is always in the downward

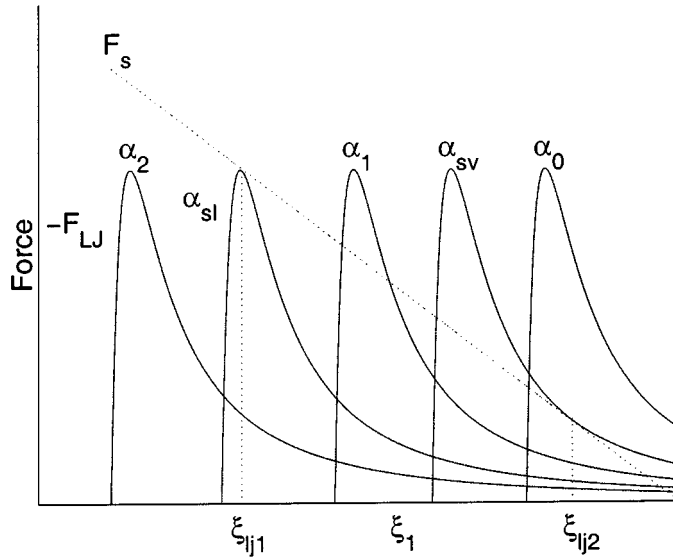


Figure 7. Spring and LJ forces for different values of α . We have $\alpha_2 > \alpha_{sl} > \alpha_1 > \alpha_{sv} > \alpha_0$.

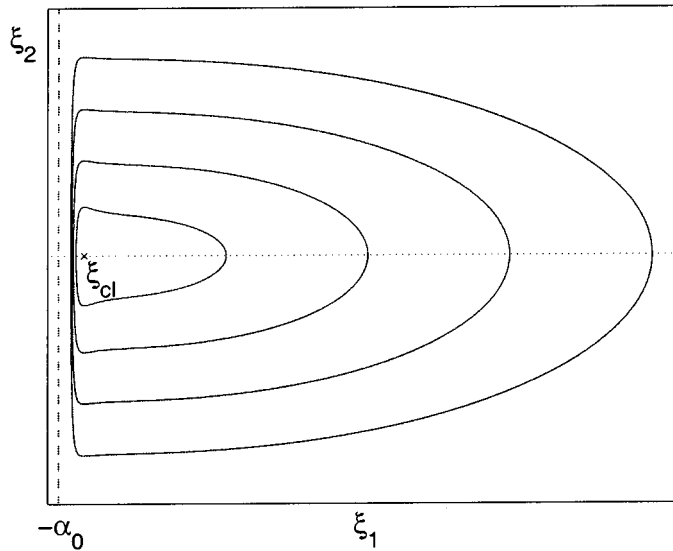


Figure 8. Phase portrait for the case $\Sigma < \Sigma_1$ and $\alpha = \alpha_0 < \alpha_{sv}$.

direction causing the tip to accelerate towards the sample until it passes the point $\xi_1 = \xi_{cl}$, where the repulsive force plus the spring force becomes larger than the vdW force, the tip is forced away from the sample. When $\alpha = \alpha_{sv}$, another fixed point appears. This is the point (ξ_{lj2}) at which the spring force is tangent to the negative of the LJ force.

We now consider the most important case, namely, $\alpha \in (\alpha_{sv}, \alpha_{sl})$. As shown in Figure 9, there are three fixed (intersection) points ξ_{cl} , ξ_{sv} and ξ_{cv} . It is evident that the linearized system (19) has purely imaginary eigenvalues at the points $\xi_1 = \xi_{cl}$ and $\xi_1 = \xi_{cv}$, whereas it has real eigenvalues with equal magnitude and opposite signs at the point $\xi_1 = \xi_{sv}$. Therefore, the fixed points $(\xi_{cl}, 0)$ and $(\xi_{cv}, 0)$ are centers while $(\xi_{sv}, 0)$ is a saddle. The corresponding phase

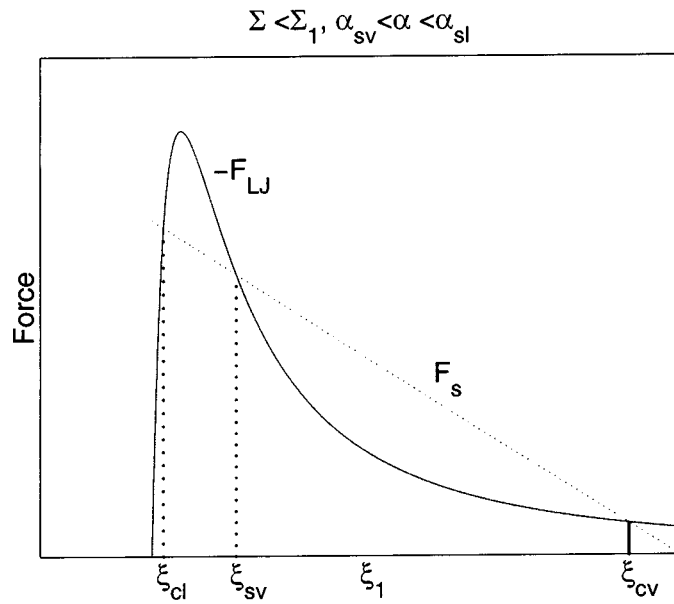


Figure 9. Spring and LJ forces for the case $\Sigma < \Sigma_1$ and $\alpha_{sv} < \alpha < \alpha_{sl}$.

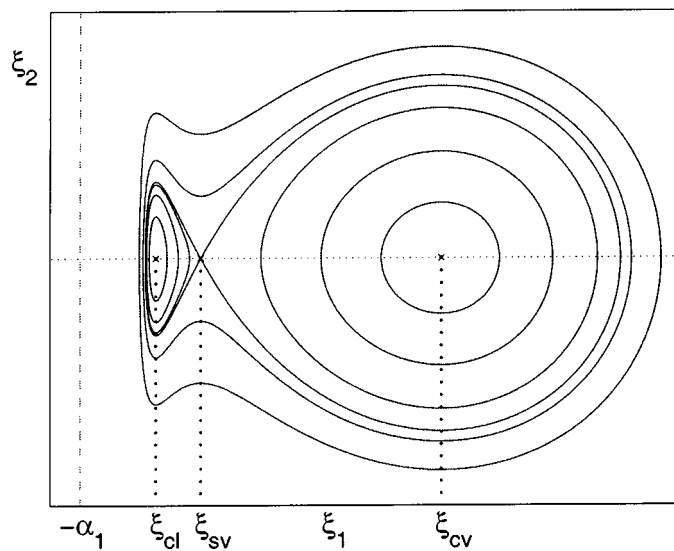


Figure 10. Phase portrait for the case $\Sigma < \Sigma_1$ and $\alpha_{sv} < \alpha_1 < \alpha_{sl}$.

portrait of the system is shown in Figure 10. There are two homoclinic orbits each connected to itself at the point $(\xi_{sv}, 0)$. The homoclinic orbit which is away from the surface is similar to the one obtained in [12] in the absence of the repulsive force. Each homoclinic orbit is filled with periodic orbits around the centers $(\xi_{cl}, 0)$ and $(\xi_{cv}, 0)$. Outside the two homoclinic orbits there are also periodic orbits. Points that are initialized on these orbits accelerate towards the sample and when they get close enough to it they are pushed back strongly by the repulsive force. The tip oscillates if it is initialized close enough to either center.

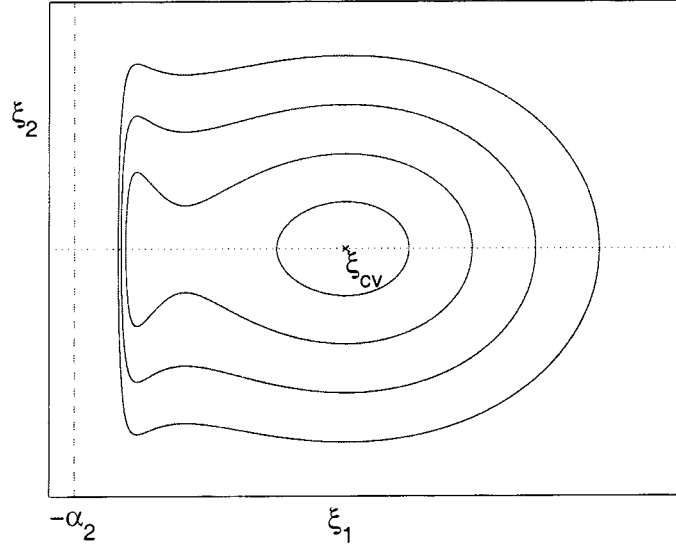


Figure 11. Phase portrait for the case $\Sigma < \Sigma_1$ and $\alpha = \alpha_2 > \alpha_{sl}$.

When $\alpha = \alpha_{sl}$, the two points ξ_{cl} and ξ_{sv} become equal. This is the value of α at which the spring force becomes tangent to the LJ force at $\xi_1 = \xi_{lj1} = \xi_{cl} = \xi_{sv}$. In this case, the homoclinic orbits no longer exist since the spring force becomes large enough to force the tip away from the surface towards the point $(\xi_{cv}, 0)$. If $\alpha > \alpha_{sl}$, we lose the fixed points ξ_{cl} and ξ_{sv} , and the only fixed point of the system is $(\xi_{cv}, 0)$. We thus lose both homoclinic orbits and the phase portrait consists only of periodic orbits around $(\xi_{cv}, 0)$ as shown in Figure 11. This is similar to the simple harmonic oscillator since the spring force becomes dominant for most of the motion. Very close to the sample the repulsive and spring forces pull the tip away from the sample. This effect is clear in Figure 11.

We now describe how to compute the values of α_{sl} and α_{sv} for a given $\Sigma < \Sigma_1$. The computation of these two values is similar, and so we give it only for $\alpha = \alpha_{sl}$ and discuss briefly the case $\alpha = \alpha_{sv}$. We know that when $\alpha = \alpha_{sl}$ the spring and LJ forces are equal at $\xi_1 = \xi_{lj1}$. Since the spring and LJ forces are equal at $\xi_1 = \xi_{lj1}$ we can find α_{sl} by solving $-F_{LJ}(\xi_{lj1}) = -\xi_{lj1}$ and $-(dF_{LJ}/d\xi_1)(\xi_{lj1}) = -1$. For numerical purposes, it is very useful to trap the value of α_{sl} in some interval. Fortunately, this can be done here as we show next. Setting the derivative of $-F_{LJ}$ equal to -1 leads to

$$15\eta^9 - 30d\eta^6 + 4\Sigma^6d = 0, \quad (20)$$

whereas $-F_{LJ}(\xi_1) = -\xi_1$ yields

$$30\eta^9 - 30\alpha\eta^8 + 30d\eta^6 - \Sigma^6d = 0. \quad (21)$$

As we mentioned above, Equations (20) and (21) are both satisfied for $\eta = \eta_{lj1}$ and $\alpha = \alpha_{sl}$. Adding these two equations and rearranging the terms, we get

$$\alpha_{sl} = 1.5\eta_{lj1} + \frac{0.1\Sigma^6d}{\eta_{lj1}^8}. \quad (22)$$

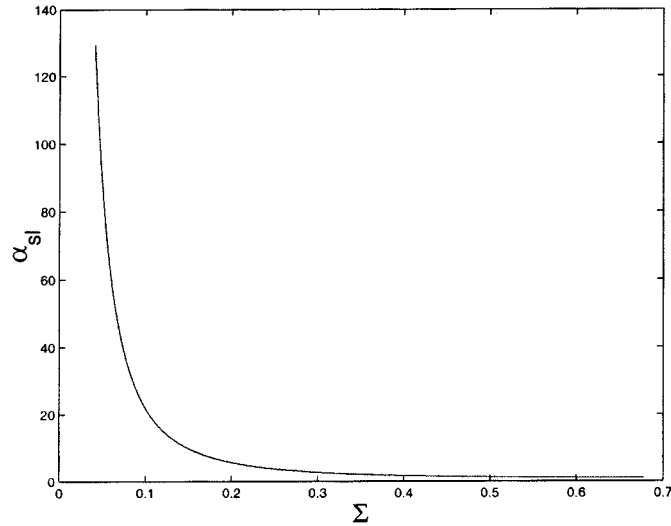


Figure 12. α_{sl} as a function of Σ . This was obtained using the bisection method to solve for the root of Equation (21) with $\eta = \eta_{lj1}$.

Using Equations (14) and (15), we obtain

$$\eta_{lj1} \in \left[\left(\frac{2}{15}\right)^{1/6} \Sigma, (0.4)^{1/6} \Sigma \right].$$

From here, the lower and upper bounds for α_{sl} can be obtained as

$$\alpha_{sll} = 1.5(0.4)^{1/6} \Sigma + \frac{0.1d}{(0.4)^{4/3} \Sigma^2} \quad (23)$$

and

$$\alpha_{slu} = 1.5\left(\frac{2}{15}\right)^{1/6} \Sigma + \frac{0.1d}{\left(\frac{2}{15}\right)^{4/3} \Sigma^2}, \quad (24)$$

respectively, where $\Sigma < \Sigma_1$. Relations (20), (21), (23) and (24) together with the bisection method can be used to locate α_{sl} which is only a function of Σ . Using this technique the results are plotted in Figure 12. Note that α_{sl} is a decreasing function of Σ . Since Σ is proportional to $k^{1/3}$, we can think of small Σ as a soft spring and large Σ as a stiff spring and the qualitative behavior of Figure 12 can be physically interpreted. For a softer spring the sample must be farther from the equilibrium position of the tip to allow the spring force to be equal to the LJ force at the point $\xi_1 = \xi_{lj1}$.

Recall that in the absence of the repulsive force, we have $\alpha_{sv} = \alpha_s = 1$. This is the case of $\Sigma \rightarrow 0$ where the LJ force is purely attractive. For larger values of Σ the negative of the LJ force becomes smaller and has a larger derivative. Therefore, α_{sv} needs to be less than 1 for the spring force to be tangent to $-F_{LJ}$ at the point $\xi_1 = \xi_{lj2}$. Furthermore, as Σ increases, the value of α_{sv} decreases. The upper bound for α_{sv} is thus equal to 1 and the lower bound is the value of α_{sv} when $\Sigma = \Sigma_1$ and is equal to 0.9828, as given later in Section 4.2. Hence, with these bounds and ξ_{lj1} replaced by ξ_{lj2} the above procedure using the bisection method can be applied to find α_{sv} . The results are shown in Figure 13. As Σ approaches Σ_1 from below α_{sl} and α_{sv} approach 0.9828 from above.

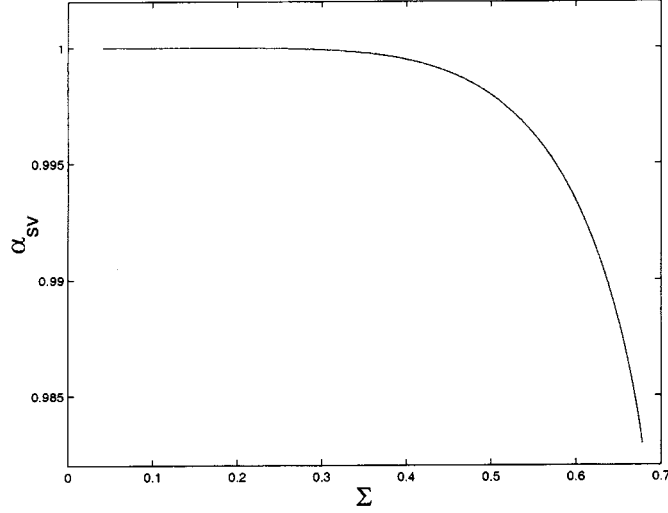


Figure 13. α_{sv} as a function of Σ . This was obtained using the bisection method to solve for the root of Equation (21) with $\eta = \eta_{j2}$.

4. Dynamics of the Forced System

In most AFMs, the cantilever motion is damped due to the surrounding air. In addition, the cantilever is forced by a sinusoidal signal $mf \cos \omega t$, where, ω takes values around the natural frequency ω_1 of the cantilever. The differential equations for the system can be written as

$$\dot{x}_1 = x_2, \quad (25)$$

$$\dot{x}_2 = -\omega_1^2 x_1 - \frac{D\omega_1^2}{(Z+x)^2} + \frac{\sigma^6 D\omega_1^2}{30(Z+x)^8} + f \cos \omega t - \mu x_2, \quad (26)$$

where we have assumed that the damping force per unit mass is μx_2 . Given a small enough ε , we let γ and δ be such that $\varepsilon\gamma = f$ and $\varepsilon\delta = \mu$. Letting the time to be a new state variable, ϕ , we have

$$\dot{x}_1 = x_2, \quad (27)$$

$$\dot{x}_2 = -\omega_1^2 x_1 - \frac{D\omega_1^2}{(Z+x)^2} + \frac{\sigma^6 D\omega_1^2}{30(Z+x)^8} + \varepsilon(\gamma \cos \phi - \delta x_2), \quad (28)$$

$$\dot{\phi} = \omega, \quad (29)$$

where $\phi(t) = \omega t + \phi_0$. Define

$$g(x_1, x_2, \phi) = \begin{pmatrix} 0 \\ \gamma \cos \phi - \delta x_2 \end{pmatrix}. \quad (30)$$

In the nondimensionalized coordinates, the perturbed system and its suspended version are given by

$$\xi_1' = \xi_2, \quad (31)$$

$$\xi_2' = -\xi_1 - \frac{d}{(\alpha + \xi_1)^2} + \frac{\Sigma^6 d}{30(\alpha + \xi_1)^8} + \varepsilon(\Gamma \cos \Omega T - \Delta \xi_2) \quad (32)$$

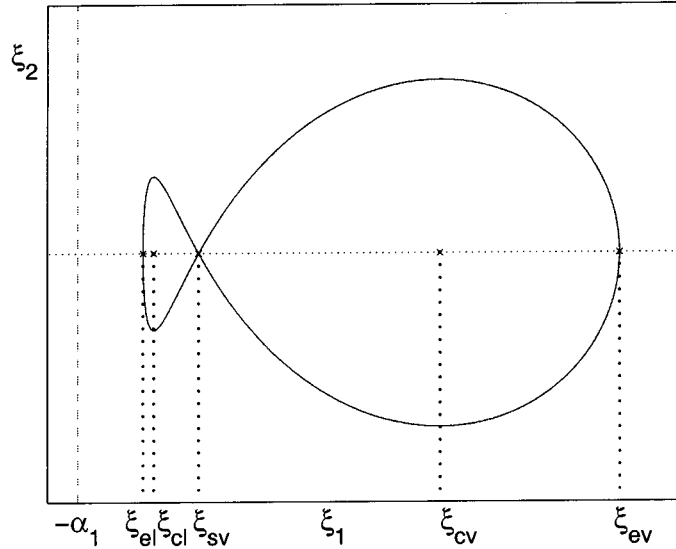


Figure 14. Homoclinic orbits of the system.

and

$$\xi'_1 = \xi_2, \tag{33}$$

$$\xi'_2 = -\xi_1 - \frac{d}{(\alpha + \xi_1)^2} + \frac{\Sigma^6 d}{30(\alpha + \xi_1)^8} + \varepsilon (\Gamma \cos \phi_n - \Delta \xi_2), \tag{34}$$

$$\phi'_n = \Omega, \tag{35}$$

where

$$\Gamma = \frac{\gamma}{\omega_1^2 Z_s}, \quad \Delta = \frac{\delta}{\omega_1}, \quad \Omega = \frac{\omega}{\omega_1} \quad \text{and} \quad \phi_n = \Omega T + \phi_{no} = \omega t + \phi_o = \phi.$$

The equations in the nondimensionalized coordinates have no explicit dependence on D and ω_1 , whereas Γ and Δ are functions of D and ω_1 . In other words, the equations have no explicit dependence on the material properties and the dimensions of the cantilever and tip. The next step is to study the dynamics of the perturbed system. To achieve this goal, we will study the Melnikov function for the perturbed system.

4.1. MELNIKOV FUNCTION

The discussion in this subsection is limited to the case $\Sigma < \Sigma_1$ and $\alpha_{sv} < \alpha < \alpha_{sl}$. Since the system that we are considering is a time-periodic perturbation of a Hamiltonian system, Melnikov's method can be used to describe how the homoclinic orbits break up in the presence of the perturbation. The homoclinic orbits of the system are shown in Figure 14. We will use the subscripts l and v to denote the left and right homoclinic orbits, respectively. Denote the solutions that start at the end points $(\xi_{el}, 0)$ and $(\xi_{ev}, 0)$ (see Figure 14) at the time origin T_0 by $(\xi_{1hl}(T - T_0), \xi_{2hl}(T - T_0))$ and $(\xi_{1hv}(T - T_0), \xi_{2hv}(T - T_0))$, respectively. If we let $\tau = T - T_0$, it can be verified that $\xi_{2hl}(\tau)$ and $\xi_{2hv}(\tau)$ are odd functions of τ .

The Melnikov function is defined by

$$M(T_0, \phi_0) = \int_{-\infty}^{\infty} DH(\xi_{1h}(\tau), \xi_{2h}(\tau))G(\xi_{1h}(\tau), \xi_{2h}(\tau), \phi_n(\tau + T_0)) d\tau, \quad (36)$$

where

$$DH(\xi_1, \xi_2) = \left(\frac{\partial H}{\partial \xi_1} \quad \frac{\partial H}{\partial \xi_2} \right)$$

with

$$\frac{\partial H}{\partial \xi_1} = \xi_1 + \frac{d}{(\alpha + \xi_1)^2} - \frac{\Sigma^6 d}{30(\alpha + \xi_1)^8} \quad \text{and} \quad \frac{\partial H}{\partial \xi_2} = \xi_2,$$

$(\xi_{1h}(\tau), \xi_{2h}(\tau))$ is either $(\xi_{1hl}(\tau), \xi_{2hl}(\tau))$ or $(\xi_{1hv}(\tau), \xi_{2hv}(\tau))$, and

$$G(\xi_1, \xi_2, \phi_n) = \begin{pmatrix} 0 \\ \Gamma \cos \phi_n - \Delta \xi_2 \end{pmatrix}. \quad (37)$$

Therefore,

$$\begin{aligned} M(T_0, \phi_0) &= \int_{-\infty}^{\infty} \xi_{2h}(\tau) (\Gamma \cos(\Omega\tau + \Omega T_0 + \phi_0) - \Delta \xi_{2h}(\tau)) d\tau \\ &= -\Delta \int_{-\infty}^{\infty} \xi_{2h}^2(\tau) d\tau + \Gamma \cos(\Omega T_0 + \phi_0) \int_{-\infty}^{\infty} \xi_{2h}(\tau) \cos \Omega\tau d\tau \\ &\quad - \Gamma \sin(\Omega T_0 + \phi_0) \int_{-\infty}^{\infty} \xi_{2h}(\tau) \sin \Omega\tau d\tau \\ &= -2\Delta \int_0^{\infty} \xi_{2h}^2(\tau) d\tau - 2\Gamma \sin(\Omega T_0 + \phi_0) \int_0^{\infty} \xi_{2h}(\tau) \sin \Omega\tau d\tau. \end{aligned}$$

The last equality holds because $\xi_{2h}(\tau)$ is an odd function of τ . By defining

$$A_d = -2 \int_0^{\infty} \xi_{2h}^2(\tau) d\tau \quad \text{and} \quad A_s = -2 \int_0^{\infty} \xi_{2h}(\tau) \sin \Omega\tau d\tau,$$

we get

$$M_{l,v}(T_0, \phi_0) = A_d \Delta + A_s \Gamma \sin(\Omega T_0 + \phi_0). \quad (38)$$

We will write $M_{l,v}$ since the Melnikov function has the same form for both homoclinic orbits of the system. The Melnikov function is a signed measure of the distance between the stable and unstable manifolds for the perturbed system. The stable and unstable manifolds intersect if the Melnikov function has simple zeros. The intersection of manifolds establishes the presence of chaos [19]. The Melnikov function given in Equation (36) will have zeros if and only if

$$\frac{\Delta}{\Gamma} \leq \left| \frac{A_s}{A_d} \right|. \quad (39)$$

Define

$$\left(\frac{\Delta}{\Gamma}\right)_{\text{cr}} = \left|\frac{A_s}{A_d}\right|. \quad (40)$$

Thus, $M(T_0, \phi_0)$ has no zeros if and only if $\Delta/\Gamma > (\Delta/\Gamma)_{\text{cr}}$. Every zero of the Melnikov function corresponds to an intersection of the stable and unstable manifolds [19]. Note that if $\Delta/\Gamma \leq (\Delta/\Gamma)_{\text{cr}}$ then the two manifolds intersect at an infinite number of points for every ϕ_0 .

The nondimensionalized system is the same as the dimensionalized one with Z replaced by α , D by d , ω_1 by 1, and σ by Σ . Hence, all of the previous analysis applies to the original system with the appropriate factors. The Melnikov function in the original coordinates is

$$M_{I,v}(t_0, \phi_0) = a_d \delta + a_s \gamma \sin(\omega t_0 + \phi_0),$$

where

$$a_d = -2 \int_0^{\infty} x_{2h}^2(\tau) d\tau \quad \text{and} \quad a_s = -2 \int_0^{\infty} x_{2h}(\tau) \sin \omega \tau d\tau.$$

x_{2h} is the second component of the homoclinic solution in the dimensionalized coordinates. Define the critical value of δ/γ as $(\delta/\gamma)_{\text{cr}} = |a_s/a_d|$. It is clear that

$$\left(\frac{\delta}{\gamma}\right)_{\text{cr}} = \frac{1}{\omega_1 Z_s} \left(\frac{\Delta}{\Gamma}\right)_{\text{cr}}. \quad (41)$$

For the homoclinic orbit on the right and in the absence of the repulsive force, $(\Delta/\Gamma)_{\text{cr}}$ was computed numerically in [12] for a range of values of values of $\alpha > 1$ and Ω around 1. As we mentioned earlier, this is a good approximation since the right homoclinic orbit is away from the sample. However, in the presence of the repulsive force, if $\alpha > \alpha_{sl}$ the saddle point is lost resulting in no homoclinic orbits and, hence, the Melnikov theory cannot be applied. Figure 15 shows the $(\Delta/\Gamma)_{\text{cr}}$ surface for the right homoclinic orbit with $\Sigma = 0.03$.

For the homoclinic orbit on the left, the results are plotted as shown in Figure 16. Note that for different values of Σ we have different Melnikov surfaces due to the change of structure of the left homoclinic orbit (see Figure 17). If the material properties and dimensions of the cantilever and tip are given, then we first compute Z_s and ω_1 and then, with the appropriate scaling, transform Figure 16 to a Figure with δ/γ , Z , and ω as coordinates.

Intersection of the stable and the unstable manifolds occurs for points which lie below the Melnikov surface. As α increases, the system tends to the spring-mass-damper system behavior.

A very interesting question arises here: can chaos exist for one of the homoclinic orbits but not for the other? By looking at Figure 18 the answer is ‘yes’ since the $(\Delta/\Gamma)_{\text{cr}}$ surfaces for the left and right homoclinic orbits do not coincide. We observe the following four regions:

1. The region of no chaos for both homoclinic orbits. This occurs when the value of Δ/Γ is large enough.
2. The region of no chaos for the left homoclinic orbit and chaos for the right homoclinic orbit. This is the region between the Melnikov surfaces for the two homoclinic orbits of the system for small enough Ω .

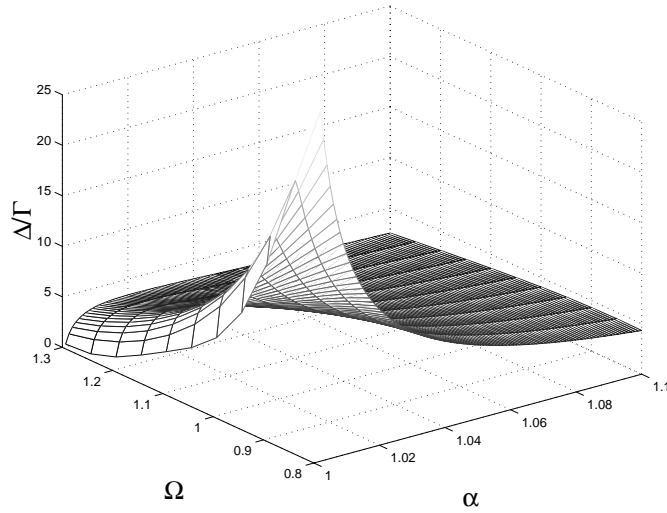


Figure 15. $(\Delta/\Gamma)_{cr}$ surface for the right homoclinic orbit with $\Sigma = 0.03$.

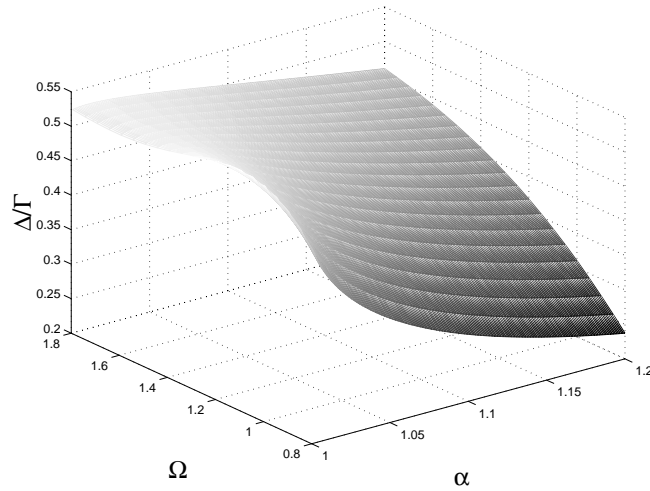


Figure 16. $(\Delta/\Gamma)_{cr}$ surface that corresponds to the left homoclinic orbit for $\Sigma = 0.03$. The region below the surface is the region where chaos exists in the system. The region above the surface is the region of no chaos.

3. The region of chaos for the left homoclinic orbit and no chaos for the right homoclinic orbit. This is the region between the Melnikov surfaces for the two homoclinic orbits of the system for large enough Ω .
4. The region of chaos for both homoclinic orbits. This occurs when the value of Δ/Γ is small enough.

4.1.1. State Feedback Control

In most AFMs, the state variable x_1 (position) is measured and the state variable x_2 (velocity) can be estimated. For the discussion here, we will assume that the velocity is available for measurement. This allows us to apply a force of the form $u = k_p x_1 + k_v x_2$ to the tip. In this case, the state equations of the system are written as

$$\dot{x}_1 = x_2,$$

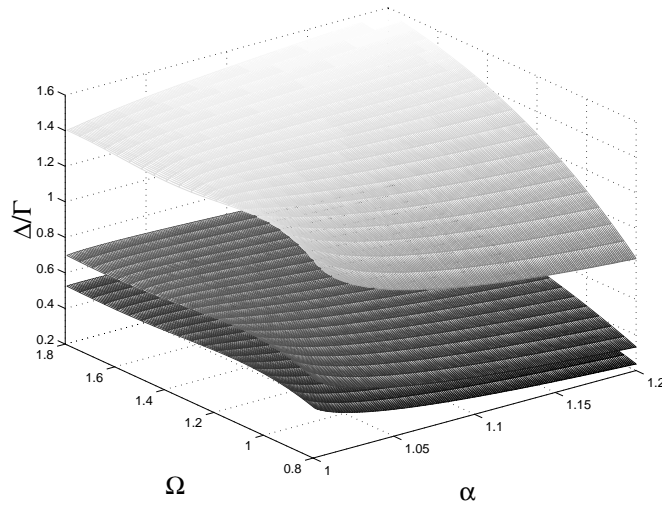


Figure 17. $(\Delta/\Gamma)_{cr}$ surfaces that correspond to the left homoclinic orbit for different values of Σ . The bottom surface corresponds to $\Sigma = 0.03$, the middle surface corresponds to $\Sigma = 0.1$, and the top surface corresponds to $\Sigma = 0.3$.

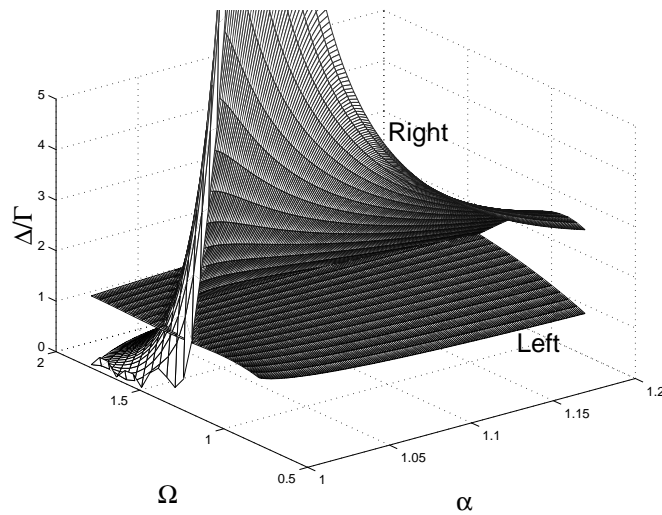


Figure 18. $(\Delta/\Gamma)_{cr}$ surfaces for the left and right homoclinic orbits with $\Sigma = 0.3$.

$$\begin{aligned} \dot{x}_2 &= -\omega_1^2 x_1 - \frac{D\omega_1^2}{(Z+x_1)^2} + \frac{\sigma D\omega_1^2}{30(Z+x_1)^8} + \varepsilon(\gamma \cos \omega t - \delta x_2) + \frac{u}{m} \\ &= -\omega_{n1}^2 x_1 - \frac{D_1 \omega_{n1}^2}{(Z+x_1)^2} + \frac{\sigma D_1 \omega_{n1}^2}{30(Z+x_1)^8} + \varepsilon(\gamma \cos \omega t - \delta_1 x_2), \end{aligned}$$

where

$$(\omega_{n1})^2 = \frac{k_1}{m} \quad \text{with} \quad k_1 = k - k_p, \quad D_1 = \frac{AR}{6k_1} \quad \text{and} \quad \delta_1 = \delta - \frac{1}{\varepsilon} \frac{k_v}{m}.$$

We can see that using k_p and k_v , we can change the parameters k and δ of the system independently. We will restrict our analysis to the case when $k_1 > 0$ and $\delta_1 \geq 0$. Since k_1 and

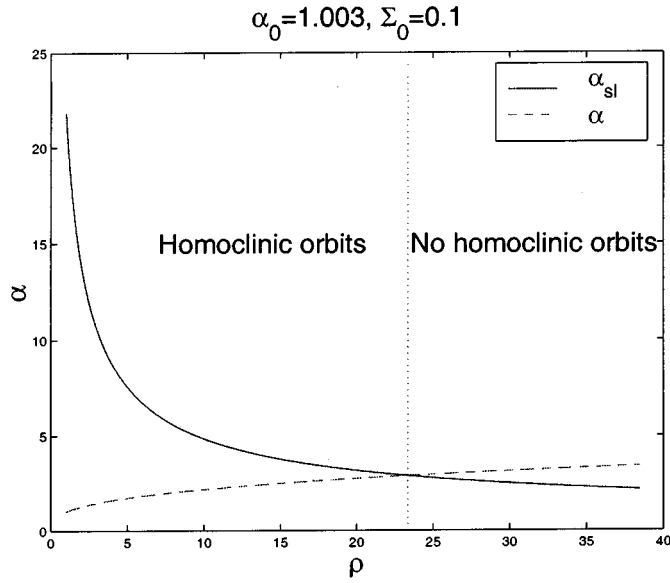


Figure 19. The range of allowable ρ . Note that the homoclinic orbits persist for $1 < \rho < \rho_{\max}$.

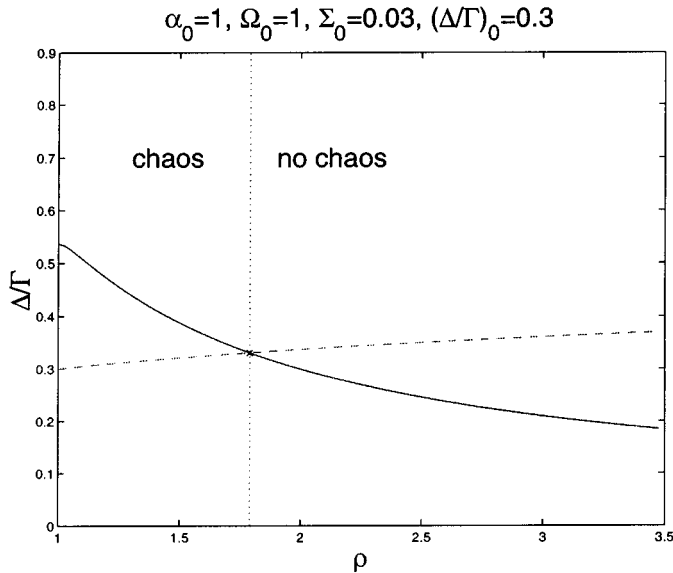


Figure 20. $\Delta/\Gamma(\rho)$ (dashed curve) and $(\Delta/\Gamma)_{\text{cr}}(\rho)$ for the left homoclinic orbit (solid curve). The two curves intersect transversely at $\rho = 1.79$. This implies that chaos exists in the system for values of ρ smaller than 1.79. If $\rho > 1.79$ chaotic motion is not possible.

δ_1 are independent, we will discuss the effect of changing each one separately. We have seen in the previous subsection that one can determine the presence of chaotic dynamics by comparing Δ/Γ with $(\frac{\Delta}{\Gamma})_{\text{cr}}(\alpha, \Omega, \Sigma)$. In Figure 17, we plot $(\frac{\Delta}{\Gamma})_{\text{cr}}(\alpha, \Omega, \Sigma)$ that correspond to the left homoclinic orbit for different values of Σ . If Δ/Γ is below the surface then chaotic dynamics is present.

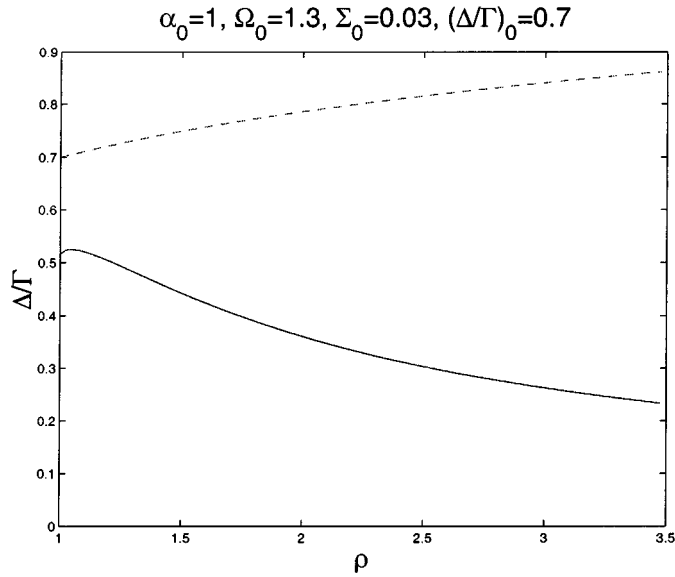


Figure 21. $\Delta/\Gamma(\rho)$ (dashed curve) and $(\Delta/\Gamma)_{cr}(\rho)$ for the left homoclinic orbit (solid curve). Chaotic motion is not possible for the whole range of ρ since $\Delta/\Gamma(\rho) > (\Delta/\Gamma)_{cr}(\rho)$.

At this point, we will consider the case of position feedback. We let $\alpha_0, \Omega_0, (\Delta/\Gamma)_0$ and Σ_0 represent nominal values of $\alpha, \Omega, (\Delta/\Gamma)$ and Σ that correspond to $k = k_0$ and $\delta = \delta_0$. The nominal point α_0 is chosen to be greater than α_{sv} and smaller than α_{sl} . Further assume that only the stiffness is being changed according to ρk_0 by varying ρ . As ρ increases, both α and Σ will increase as a function of $\rho^{1/3}$. As we discussed earlier, as long as α is less than α_{sl} the homoclinic orbits persist. In addition, recall that as ρ increases the upper bound α_{sl} decreases, see Figure 12. Therefore, we will allow ρ to increase only up to the maximum value ρ_{max} that guarantees the persistence of the homoclinic orbits; that is ρ is greater than 1 and less than ρ_{max} , see Figure 19. For $k = \rho k_0$,

$$\left(\frac{\Delta}{\Gamma}\right)_{cr}(\alpha, \Omega, \Sigma) = \left(\frac{\Delta}{\Gamma}\right)_{cr}(\rho^{1/3}\alpha_0, \rho^{-1/2}\Omega_0, \rho^{1/3}\Sigma_0) := \left(\frac{\Delta}{\Gamma}\right)_{cr}(\rho)$$

and

$$\frac{\Delta}{\Gamma}(\rho) := \rho^{1/6} \left(\frac{\Delta}{\Gamma}\right)_0.$$

We will call the plot of $\rho^{1/6}(\Delta/\Gamma)_0$ as a function of ρ a control curve. In Figures 20 and 21, we plot $(\Delta/\Gamma)_{cr}(\rho)$ for the left homoclinic orbit and a control curve. Note that in Figure 20 for $\rho < 1.79$, chaos is present in the system. For values of ρ greater than 1.79, chaotic behavior of the cantilever is not possible in the sense of Melnikov. In this case, the possibility of chaos can be eliminated by position feedback control. In Figure 21 chaos is not possible for the whole range of ρ .

Now, we are going to show that the operating point of the tip-sample system can be moved from certain regions to other regions via state feedback control (the regions are described in the previous subsection). Figures 22 and 23 show the control curves (position control only) along with the $(\Delta/\Gamma)_{cr}(\rho)$ curves for both the right and left homoclinic orbits. In Figure 22,

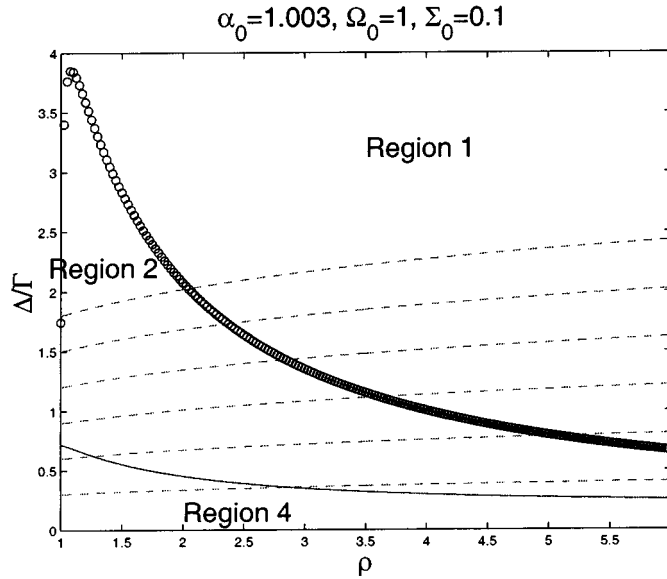


Figure 22. Using position feedback control to move the operating point from region 4 to region 2 and region 2 to region 1. The curve with the marker 'o' is $(\Delta/\Gamma)_{cr}(\rho, \alpha_0, \Omega_0, \Sigma_0)$ for the right homoclinic orbit, the solid curve is $(\Delta/\Gamma)_{cr}(\rho, \alpha_0, \Omega_0, \Sigma_0)$ for the left homoclinic orbit, and the dashed curves are the control curves. The boundaries of the different regions are the $(\Delta/\Gamma)_{cr}$ surfaces for the right and left homoclinic orbits.

note that the operating point can be moved between regions 4 and 2 which means that the possibility of chaos can be eliminated for the left homoclinic orbit while the right homoclinic orbit still exhibits chaotic behavior. It is also possible to eliminate the possibility of chaos for both homoclinic orbits if it exists with $u = 0$. As we can see in the case of Figure 22, this possibility is eliminated for the left homoclinic orbit before the right homoclinic orbit as the value of ρ increases. In addition, as in [12], the possibility of chaos can be eliminated for the right homoclinic orbit using position feedback control. This is represented by the control curves that cross from region 2 to region 1.

More interesting transitions between different regions take place as shown in Figure 23. We note the following different behaviors when position feedback control is applied:

1. The transition from region 3 to region 4 then to region 2 as the value of $k_1 = k - k_p$ increases. This implies that if chaos exists for both homoclinic orbits, it is possible to be eliminated for only one of the homoclinic orbits, i.e., increasing $k_1(\rho)$ eliminates the possibility of chaos for the left homoclinic orbit, whereas decreasing $k_1(\rho)$ eliminates chaos for the right homoclinic orbit.
2. The transition from region 3 to region 4, then region 4 to region 2, and then region 2 to region 1 as the value of k_1 increases. This means that the possibility of chaos can be eliminated for both homoclinic orbits.
3. The transition from region 3 to region 1, then region 1 to region 2, and then region 2 to region 1 as the value of k_1 increases. It is interesting that chaos can be eliminated from only one homoclinic orbit while keeping the other one nonchaotic.
4. Note that there exists a control curve that will cross directly from region 3 to region 2 without passing region 1 or region 4. This means that chaos can be interchanged between the two homoclinic orbits without passing through another dynamical behavior. If k_1 is

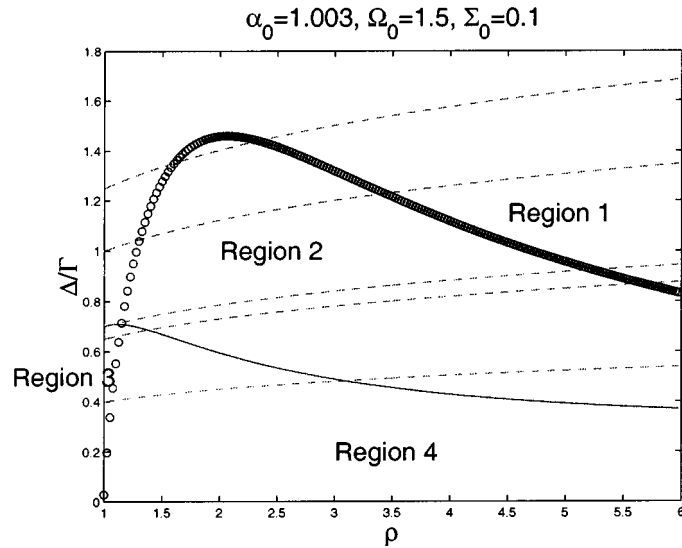


Figure 23. Using position feedback control to move the operating point from region 3 to region 4 to region 2, region 1 to region 2 then back to region 1 and region 3 to region 1 to region 2.

large enough this control curve exits to region 1 which is the region of no chaos for both homoclinic orbits.

5. As was shown in [12], the possibility of chaos can be eliminated for the right homoclinic orbit through position feedback control. This is represented by the curve that crosses from region 2 to region 1.

Now, we fix $k = k_0$ and let $\delta = \rho\delta_0$. This gives the point $(\alpha_0, \Omega_0, \rho(\Delta/\Gamma)_0)$. So varying ρ causes the operating point to move in the vertical (Δ/Γ) direction. It is easy to note that changing the damping in the system does not change the value of Σ and, hence, the $(\Delta/\Gamma)_{cr}$ surface is fixed. Thus, we can move the operating point from one side of the $(\Delta/\Gamma)_{cr}$ surface for a given Σ to the other by changing δ appropriately. As one expects, increasing the damping in the system eliminates the possibility of chaos. For the surfaces plotted in Figure 18 as we increase the damping δ_1 the corresponding vertical lines move from region 4 to region 1 passing through region 2 or region 3 or directly (if they cross the one dimensional intersection curve of the two surfaces). The transition between regions 2 and 3 is not possible in this case.

We conclude that given a specified cantilever, it is possible to design a controller of the form $u = k_v x_1 + k_p x_2$ that will eliminate chaos if it exists when $u = 0$.

4.2. THE CASE $\Sigma \geq \Sigma_1$

When $\Sigma = \Sigma_1$ the slope of $-F_{LJ}$ at $\xi_1 = \xi_{ljs}$ is equal to -1 and is minimum. In this case, $\alpha_{sl} = \alpha_{sv}$. Due to the fact that we know the point at which the slope of $-F_{LJ}$ is equal to -1 , we can compute α_{sl} . The spring force must be equal to the LJ force at $\xi_1 = \xi_{ljs}$ when $\alpha = \alpha_{sl}$. Using this fact together with Equation (15), we have

$$-\xi_{ljs} = \alpha_{sl} - (\alpha_{sl} + \xi_{ljs}) = \frac{11}{12} \frac{d}{(\alpha_{sl} + \xi_{ljs})^2}.$$

Table 1. Summary of the dynamical behavior of the system.

Σ	α	Fixed points	Phase portrait
$\Sigma < \Sigma_1$	$\alpha < \alpha_{sv}$	1 center	Figure 8
	$\alpha = \alpha_{sv}$	1 center, 2 nonhyperbolic	–
	$\alpha_{sv} < \alpha < \alpha_{sl}$	2 centers, 1 saddle	Figure 10
	$\alpha = \alpha_{sv}$	1 center, 2 nonhyperbolic	–
	$\alpha > \alpha_{sl}$	1 center	Figure 11
$\Sigma = \Sigma_1$	$\alpha < \alpha_{sv,sl}$	1 center	–
	$\alpha = \alpha_{sv,sl}$	1 center, 2 nonhyperbolic	–
	$\alpha > \alpha_{sv,sl}$	1 center	–
$\Sigma > \Sigma_1$	all	1 center	–

Therefore,

$$\alpha_{sl} - (0.4)^{1/6} \Sigma_1 = \frac{11}{12} \frac{d}{((0.4)^{1/6} \Sigma_1)^2}.$$

Solving for α_{sl} , we get $\alpha_{sl} = 0.9828$.

If $\Sigma > \Sigma_1$, the slope of $-F_{LJ}$ at $\xi_1 = \xi_{ljs}$ is greater than -1 which indicates that the spring force cannot be tangent to the negative of the LJ force. Thus, the intersection of the spring and LJ forces is always transversal and it happens only once. This gives the position of the only fixed point of the system which is of center type stability.

5. Conclusions

The experimental observation that the motion of the microcantilever (which is the heart of the detection scheme employed by atomic force microscopes) can be chaotic led to the dynamical analysis of the cantilever-sample system in the AFM. An appropriate mathematical model for this system was needed in order to understand the dynamical behavior of the cantilever. To this end, the cantilever-sample interaction was modeled via Lennard–Jones potential. Using this model, it is shown that it is possible for chaos to exist in the system depending on the extent of damping, forcing, and equilibrium position of the cantilever. The region in the space of physical parameters in which chaos exists was found. It was shown that state feedback control can be used to eliminate the possibility of chaos.

Acknowledgement

This research was supported by the National Science Foundation under Grants No. ECS-9632820, ECS-9733802, and AFOSR under Grant No. F49620-97-1-0168.

References

1. Binnig, G., Quate, C. F., and Gerber, C., ‘Atomic force microscope’, *Physical Review Letters* **56**(9), 1986, 930–933.

2. Strausser, Y. E., Schroth, M., and Sweeney III, J. J., 'Characterization of the low-pressure chemical vapor deposition grown rugged polysilicon surface using atomic force microscopy', *Journal of Vacuum Science and Technology A* **15**(3), 1997, 1007–1013.
3. Zhong, Q., Inniss, D., Kjoller, K., and Elings, V. B., 'Fractured polymer/silica fiber surface studied by tapping mode atomic force microscopy', *Surface Science* **290**(1–2), 1993, L688–L692.
4. Hoh, J. H., Lal, R., John, S. A., Revel, J. P., et al., 'Atomic force microscopy and dissection of gap junctions', *Science* **253**, 1991, 1405–1408.
5. Kasas, S., Thomson, N. H., Smith, B. L., Hansma, H. G., et al., 'Escherichia coli rna polymerase activity observed using atomic force microscopy', *Biochemistry* **36**(3), 1997, 461–468.
6. Williams, C. C. and Wickramasinghe, H. K., 'High resolution thermal microscopy', in *IEEE 1986 Ultrasonics Symposium Proceedings*, Vol. 1, B. R. McAvoy (ed.), IEEE, New York, 1986, pp. 393–397.
7. Babcock, K., Dugas, M., Manalis, S., and Elings, V., 'Magnetic force microscopy: Recent advances and applications', in *Evolution of Thin Film and Surface Structure and Morphology Symposium, Materials Research Society*, B. G. Demczyk, E. E. Garfunkel, B. M. Clemens, E. D. Williams, et al. (eds.), 1995, pp. 311–322.
8. Grutter, P., Rugar, D., and Mamin, H. J., 'Magnetic force microscopy of magnetic materials', *Ultramicroscopy* **47**(4), 1992, 393–399.
9. Terris, B. D., Stern, J. E., Rugar, D., and Mamin, H. J., 'Localized charge force microscopy', *Journal of Vacuum Science and Technology* **8**(1), 1990, 374–377.
10. Slinkman, J. A., Williams, C. C., Abraham, D. W., and Wickramasinghe, H. K., 'Lateral dopant profiling mos structures on a 100 nm scale using scanning capacitance microscopy', in *International Electron Devices Meeting 1990, Technical Digest*, San Francisco, CA, December, 1990, pp. 73–76.
11. Sarid, D., *Scanning Force Microscopy*, Oxford University Press, New York, 1994.
12. Ashhab, M., Salapaka, M. V., Dahleh, M., and Mezić, I., 'Control of chaos in atomic force microscopes', in *American Control Conference*, Albuquerque, New Mexico, June, 1997, pp. 192–202.
13. Burnham, N. A., Kulik, A. J., Gremaud, G., and Briggs, G. A. D., 'Nanosubharmonics: The dynamics of small nonlinear contacts', *Physical Review Letters* **74**, 1995, 5059–5092.
14. Cleveland, J. P., 'Measuring and understanding forces on atomic length scales with the atomic force microscope', Ph.D. Dissertation, University of California at Santa Barbara, 1995.
15. Walters, D. A., Cleveland, J. P., Thomson, N. H., Hansma, P. K., et al., 'Short cantilevers for atomic force microscopy', *Review of Scientific Instruments* **67**(10), 1996, 3583–3590.
16. Hutter, J. L. and Bechhoefer, J., 'Calibration of atomic-force microscope tips', *Review of Scientific Instruments* **64**(7), 1993, 1868–1873.
17. Salapaka, M. V., Bergh, H. S., Lai, J., Majumdar, A., and McFarland, E., 'Multimode noise analysis of cantilevers for scanning probe microscopy', *Journal of Applied Physics* **81**(6), 1997, 2480–2487.
18. Israelachvili, J. N., *Intermolecular and Surface Forces*, Academic Press, Boston, MA, 1985.
19. Wiggins, S. *Introduction to Applied Nonlinear Dynamical Systems and Chaos*, Springer-Verlag, Berlin, 1990.